Plasmonic gold nanoshell induced spectral effects and refractive index sensing properties of excessively tilted fiber grating

Binbin Luo (罗彬彬)*, Huafeng Lu (卢化锋), Shenghui Shi (石胜辉)**,
Mingfu Zhao (赵明富), Jiao Lu (鲁 姣), Yajie Wang (王亚杰), and Xin Wang (王 鑫)

Chongqing Key Laboratory of Optical Fiber Sensor and Photoelectric Detection, Chongqing University of Technology,
Chongqing 400054, China
*Corresponding author: luobinbin@cqut.edu.cn; **corresponding author: Shshill@cqut.edu.cn
Received July 13, 2018; accepted August 30, 2018; posted online September 25, 2018

We demonstrate a fiber refractive index (RI) sensor based on an excessively tilted fiber grating (ExTFG) immobilized by large-size plasmonic gold nanoshells (GNSs). The GNSs are covalently linked on ExTFG surface. Experimental results demonstrate that both the intensity of the transverse magnetic (TM) and transverse electric (TE) modes of ExTFG are significantly modulated by the localized surface plasmon resonance (LSPR) of GNSs due to the wide-range absorption band. The wavelength RI sensitivities of the TM and TE modes in the low RI range of 1.333–1.379 are improved by ∼25% and ∼14% after GNSs immobilization, respectively, and the intensity RI sensitivities are ∼599%/RIU and ∼486%/RIU, respectively.

OCIS codes: 060.2370, 120.0280, 060.3735.
doi: 10.3788/COL201816.100603.

Owing to the advantages of compact size, high sensitivity, and capability of remote sensing, refractive index (RI) sensors based on optical fiber have been widely used in the biochemical sensing field, including tapered fiber[1], micronano fiber[2], photonic crystal fiber (PCF)[3], etched or D-shape fiber Bragg gratings (FBGs)[4,5], long period fiber gratings (LPFGs)[6], tilted fiber Bragg gratings (TFBGs)[7], and excessively tilted fiber grating (ExTFG)[8] based RI sensors, etc. Therefore, the fiber grating sensors are of great interest due to their ability to be modulated/demodulated by resonance wavelength or intensity.

In order to achieve an enhancement in the sensitivity for surrounding RI (SRI), combining the small size and flexibility of optic fiber with noble metal film to establish the excellent RI sensitivity of the surface plasmon resonances (SPR) sensors is extensively studied in the biosensing field[9]. Compared with SPR, the unique optical property of supporting localized SPR (LSPR) by noble metal nanoparticles has attracted greater interest, which is attributed to the fact that LSPRs are much more localized, allowing for probing processes at the platform interface with spatial sensitivities well within the nanometer scale[10,11].

To excite the LSPR of noble metal nanoparticles by the propagating optical mode in a fiber waveguide, the fields of mode and plasmonic resonance need to strongly overlap. For this purpose, several schemes of an optic fiber evanescent wave-based LSPR sensor have been developed. The earliest and most typical one is a tapered optical fiber LSPR sensor[12]; Cao *et al.*[13] reported an LSPR probe using an unclad optical fiber biosensor immobilized with gold nanospheres (∼60 nm) and gold nanorods (ratio of 4:1); Brenda *et al.*[14] immobilized ensembles of gold nanospheres (∼45 nm) within tailored areas on the open side of an exposed-core microstructured fiber yielding a monolithic, highly sensitive plasmon-based RI sensor. As for the fiber grating-based LSPR, Lepinay *et al.*[15] developed either gold nanocage (AuNC) or gold nanosphere (AuNS)-based TFBG–LSPR sensors for biosensing. The above nanoparticle-enhanced LSPR studies are mainly focused on the use of gold nanoparticles with a size smaller than 100 nm, which usually have a maximal absorbance in colloidal solution in the visible wavelength range (400 nm–700 nm). Lao *et al.*[16] demonstrated a very novel and sensitive TFBG–SPR–LSPR biosensor, where the sensing mechanism is that the LSPR of ∼17 nm gold nanospheres in the near-infrared (NIR) was excited by the long-range SPR of 50 nm gold film coated on a TFBG sensor, but not directly excited by the normal evanescence field of the TFBG. However, the maximum absorbance of the LSPR of some gold nanoparticles, such as AuNC and gold nanoshells (GNSs), is in the NIR range depending on the size and porosity of the particles. Especially for the GNSs with a large size, the absorbance band can extend to the C-L band by adjusting the diameter and internal diameter ratio[17]. Burgmeier *et al.*[18] immobilized GNSs on the surface of an etched FBG with a diameter of ∼6 μm through an electrostatic bond, showing an extremely high intensity RI sensitivity induced from localized electromagnetic hot spots in the gaps between the GNS clusters, where the local electric field is enhanced by many orders of magnitude.

However, the study and work presented herein is the first known report of coupling an excessively tilted fiber grating with large-size GNSs for the fabrication of an LSPR sensor in the NIR wavelength range. An ExTFG

is similar to an LPFG since it can couple light from the core mode to the co-propagating high-order cladding modes, and thus, unlike FBG, it is intrinsically sensitive to SRI without the need for the cladding etching process[19]. But ExTFGs have much smaller grating periods (∼30 μm) than LPFGs, thus possessing a higher RI sensitivity and a much lower thermal cross talk effect as compared to the conventional LPFGs, and even a lower temperature sensitivity (∼5 pm/°C) than normal FBGs (∼10 pm/°C)[19]. The goal of this study is to determine the spectral effects and RI sensing characteristics induced by the large-size GNSs with an ExTFG, which may have applications in novel fiber grating-based LSPR biochemical sensors.

The ExTFG was fabricated in H_2-loaded SM28 fiber by using scanning mask technique and doubled frequency Ar^+ laser emitting at 244 nm with a power level of ∼150 mW; a custom-designed amplitude mask (period of 6.6 μm) was tilted at 78° thus producing ∼81° excessively tilted fringes. The spectrum resulting from a certain polarized light of the fabricated ExTFG in NIR (1250 nm–1650 nm) is shown in Fig. 1(a). Due to the introduction of excessively tilted fringing, the significant birefringence would cause a dual-peak resonance in each cladding mode that corresponds to the transverse magnetic (TM) and transverse electric (TE) mode, respectively. Fig. 1(b) is the polarization dependence spectra of peak '1' shown in Fig. 1(a) that was measured in a zoomed wavelength range between 1255 and 1275 nm. The phase-matching condition of an ExTFG could be expressed as[20]

$$\lambda_{i,\text{clad}}^m = (n_{\text{eff,core}} - n_{i,\text{eff,clad}}^m)\Lambda_g / \cos\theta, \qquad i = \text{TE or TM},$$
(1)

where $n_{\text{eff,core}}$, and $n_{i,\text{eff,clad}}^m$ are the effective indices of the core mode and the mth cladding mode, respectively; Λ_g is the nominal grating period; θ is the tilt angel, and $\lambda_{i,\text{clad}}^m$ represents the resonance wavelength of the mth cladding mode (TM or TE).

Gold-nanoshell dispersion liquid (3.2×10^{10} particles/mL) was purchased from Beijing DK Nanotechnology Co., Ltd., China. The GNS is composed of a gold nanoparticle layer around a SiO_2 core, whose optical properties

Fig. 2. (a) Size distribution and (b) absorption spectrum of the GNSs.

can be rationally tuned over a broad spectral range through the ratio of the gold layer thickness to the total diameter[21]. Figures 2(a) and 2(b) are the size distribution and the extinction spectrum of the used GNSs, respectively, showing that the GNSs have a total diameter of ∼155 nm and a peak resonance wavelength of ∼781 nm with an extinction spectrum covering from 400 nm to 1600 nm. Since the extinction spectrum of GNSs overlaps with the cladding mode resonance spectrum of ExTFG in the NIR range [Fig. 1(a)], the evanescence of the cladding modes can efficiently interact with the GNSs on the fiber surface and excite the LSPR.

The immobilization of GNSs on the fiber surface was conducted by the following sequences. First, the ExTFG was immersed in HNO_3 (5% volume fraction, in ethanol) solution for 1 h, followed by being washed with de-ionized water and ethanol. Second, it was incubated in NaOH solution (300 μL, 8 mg/mL) for 3.5 h at 40°, and subsequently 0.5 h at room temperature after being washed with de-ionized water and then dried in air. This step is to activate hydroxyl groups on the fiber surface. Third, the silanization of the fiber surface was realized by immersing the hydroxyl-activated ExTFG in a 3-mercaptopropyltrimenthoxy silane (MPTMS) (1% in glacial acetic acid) solution for 10 min at 65°. This step made a layer of sulfydryl ('-SH') exposed outside the fiber surface. Finally, the silaned ExTFG was incubated in the prepared GNS suspension (400 μL, 2 mg/mL) for ∼1 h, where the GNSs were combined to the fiber surface through covalent bonds (i.e., 'Au-S' bond), and then it was washed with ultrapure water and ethanol to remove the non-bonded GNSs. The linking mechanism of GNSs on the fiber surface is depicted in Fig. 3. A field emission scanning electron microscope (SEM) (ZEISS SIGMA HD) was used to assess the coating effect of GNSs on the
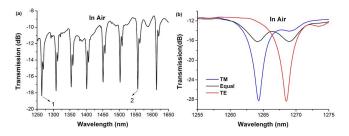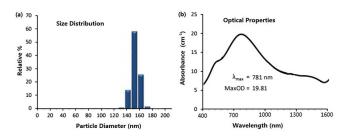

Fig. 1. (a) Whole spectrum of the ExTFG with a certain polarized light in the wavelength range of 1250 nm to 1650 nm, and (b) polarization dependence spectra for the zoomed peak '1' between 1255 nm and 1275 nm, blue: TM polarization, red: TE polarization, black: equal polarization.
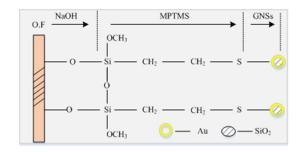

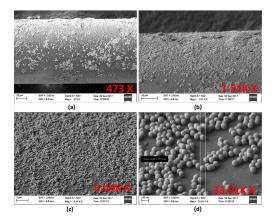Fig. 3. Linking mechanism of the GNS-immobilized ExTFG.

Fig. 4. SEM images of the GNS-immobilized ExTFG: (a) 473×, (b) 1510×, (c) 5440×, and (d) 33910×.

ExTFG surface. As shown in Figs. 4(a)–4(d), surface modification is evident, demonstrating the mass of GNSs being immobilized on the fiber surface.

The experimental setup to monitor spectra of the GNS-immobilized ExTFG is shown in Fig. 5. Light from a broadband source (BBS, 1250 nm–1650 nm) was launched into the fiber and transmitted to a polarizer to form linearly polarized light, and a polarization controller (PC) was used to adjust the polarization of the probing light. The transmission spectrum was recorded by an optical spectrum analyzer (OSA, MS9740 A, 600 nm–1700 nm, 0.03 nm).

Figure 6(a) shows the spectra of the ExTFG in air before and after GNS immobilization, and we can see clearly that TM mode shows a larger wavelength redshift (0.9 nm) than the TE mode (0.7 nm), which demonstrates a larger change to the effective index of the TM mode than that of the TE mode. However, both the TM and TE
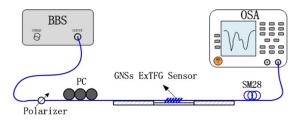

Fig. 5. Experimental setup to monitor the spectra of the ExTFG or GNS-immobilized ExTFG.
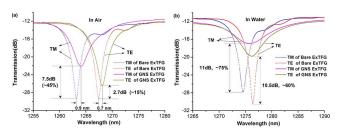

Fig. 6. Spectral effect of GNSs immobilized on the ExTFG (a) in air and (b) in water.

modes suffer obvious attenuation in peak intensity, indicating the effective coupling that occurred between the ExTFG and GNSs. The peak attenuation mainly stemmed from the localized surface plasmon polaritons (SPPs) of the GNSs due to the wide-range absorption band [Fig. 2(b)]. In addition, the peak attenuation (7.5 dB, ~45%) of the TM mode is about 3 times larger than that (2.7 dB, ~15%) of the TE mode. Since the real part [i.e., $\mathrm{Re}(n_{\mathrm{eff}})$] and the imaginary part [i.e., $\mathrm{Im}(n_{\mathrm{eff}})$] of the effective index of the cladding mode represent the propagation and absorption properties of the ExTFG, respectively, this means that there was a much larger change to the $\mathrm{Im}(n_{\mathrm{eff}})$ of the TM mode than that of the TE mode when the ExTFG was immobilized with GNSs. It is also necessary to mention that the spectra of the TM and TE modes cannot be tuned back to the original position by changing the polarized status of the input light, thus the effect of the GNSs immobilization on the spectra of ExTFG is polarization independent. This is due to the fact that the optical properties of GNSs are untunable, and once GNSs have been immobilized on a fiber surface the mode field of the ExTFG will be permanently changed by the GNSs.

In order to check the spectral effect of SRI on the proposed LSPR sensor, we immersed the bare and the GNS-immobilized ExTFGs in water, respectively. As shown in Figs. 6(a) and 6(b), on one hand, it is clear that the intensities of the TM and TE modes of the bare ExTFG are nearly unchanged when it is transferred from air to water, but those of the GNS-immobilized ExTFG dramatically attenuate due to the enhancement of LSPR absorption of the GNSs induced by the SRI increasing (1.0 to 1.333). On the other hand, we can see from Fig. 6(b) that the peak intensity differences of the TM and TE modes between the bare ExTFG and GNS-immobilized one in water are ~11 dB (~75%) and ~10.5 dB (~60%), respectively, which are much larger than the differences in air [Fig. 6(a)], indicating that the modulation of GNSs to the $\mathrm{Im}(n_{\mathrm{eff}})$ of the TM and TE modes becomes larger in a higher SRI environment. In addition, the wavelength separations between the TM and TE modes of the ExTFGs become smaller when transferred from air to water as a result of the shifting of the TM peak induced by the increase of SRI being faster than that of the TE mode, which can be explained by the decreasing effective index difference between the TM and TE modes[19]. The tendency is much more obvious for the GNS-immobilized ExTFG, as can be seen from Fig. 6(b), and the peaks of the TM and TE modes are nearly combined.

The RI sensing characteristics of the ExTFG before and after GNS immobilization were examined by using a series of RI liquids ranging from 1.3331 to 1.37935. As shown in Figs. 7(a) and 7(b), the spectra of the TM and TE modes of the bare ExTFG redshift with a peak intensity becoming slightly deepened, while the spectra of the GNS-immobilized ExTFG have a similar wavelength variation manner but with opposite intensity evolution; that is, the peak intensity suffers an obvious decrease and the
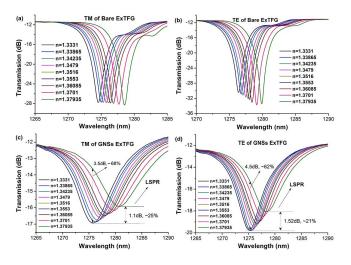
Fig. 7. Spectral evolution in the SRI range of 1.3331–1.37935 for (a) the TM mode and (b) the TE mode of the bare ExTFG; (c) the TM mode and (d) the TE mode of the GNS-immobilized ExTFG.

bandwidth broadens with increasing SRI [Figs. 7(c) and 7(d)]. The observed phenomenon demonstrates that the coupling strength from the evanescence field of ExTFG to GNSs becomes larger when the SRI increases, thus gradually leading to a spectrum that is too loose to build strong resonance along the grating.

For clarity, we depict the resonance wavelength and normalized intensity evolutions that correspond to Fig. 7 in Fig. 8. We can see clearly from Fig. 8(a) that the wavelength RI sensitivities of the TM and TE modes increase from 85.38 nm/RIU to 106.07 nm/RIU (i.e., ~25%) and from 74.62 nm/RIU to 85.4 nm/RIU (i.e., ~15%) after GNSs immobilization, respectively, indicating that the induced variation in $\mathrm{Re}(n_{\mathrm{eff}})$ of the TM and TE modes by the change of SRI for the GNS-immobilized ExTFG is greater than those of the bare ones, which could be attributed to the fact that the additional nanoparticles (i.e., GNSs) on the ExTFG surface would result in the enhancement in the overlap between the evanescence of the cladding modes and the surrounding medium (and also more in the TM mode than in the TE mode).

Figures 7(c) and 7(d) show that the normalized intensity variations of the TM and TE modes of the GNS-immobilized ExTFG with SRI are nearly the same
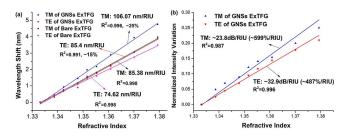

Fig. 8. (a) Corresponding resonance wavelength shift of the bare ExTFG and the GNS-immobilized ExTFG, and (b) the normalized intensity variation of the GNS-immobilized ExTFG in the SRI range of 1.3331–1.37935.

(~25% and ~21%, respectively) in the RI range of 1.3331 to 1.37935, and the corresponding intensity RI sensitivities of the TM and TE modes are calculated to be ~23.8 dB/RIU (~599%/RIU) and ~32.9 dB/RIU (~487%/RIU) with a good linearity ($R^2 > 0.98$) in this low RI range [Fig. 8(b)], respectively. In order to obtain a higher intensity RI sensitivity, the single-frequency light emitting at the wavelength of the TM or TE peak combined with a photodetector could be adopted, then the intensity variations of the TM and TE peaks would be 3.5 dB (~68%) and 4.5 dB (~62%), respectively, as illustrated in Figs. 7(c) and 7(d), and the intensity RI sensitivities of the TM and TE modes in this case are estimated to be as high as ~76 dB/RIU (~1500%/RIU) and ~97 dB/RIU (~1350%/RIU), respectively.

However, it can be still seen from Figs. 4(a)–4(d) that the GNSs on the fiber surface are not so uniform. This is because the sodium citrate around the GNSs has been removed before using, and thus GNSs would partially cluster when they were immobilized on the fiber surface. Since this nonuniformity would decrease the effective interaction area between the GNSs and the evanescence field of the ExTFG, the above obtained sensitivity improvement of the ExTFG–LSPR sensor would be further enhanced by reducing the nonuniformity of the GNSs on the fiber surface.

In our previous study[22], we used gold nanospheres with a diameter of ~20 nm to modify the surface of the ExTFG, showing that the improvement in the wavelength RI sensitivity is only ~5%, and also the influences of these small-size gold nanospheres on the intensity of the TM and TE modes of the ExTFG are much weaker than those obtained in this work. Therefore, the comparisons confirm again that the induced LSPR effect of large-size GNSs by ExTFG is much better than that of small-size gold nanospheres, since the peak resonance wavelength of the GNSs is much closer to the cladding mode resonance spectrum of the ExTFG in the NIR range (1250 nm–1660 nm).

Furthermore, we also inspected the localized SPP effects on the polarization dependence spectrum in a longer wavelength range of the GNS-immobilized ExTFG. We selected the spectrum of peak '2' in Fig. 1(a), which is in the C-L band. We found that the spectra in the C-L band have similar spectral effect and RI sensing characteristics to those in the shorter wavelength range, but the intensity attenuations of the TM and TE modes in the C-L band are much weaker than those in the shorter wavelength range. The improvement in the wavelength RI sensitivities of the TM and TE modes is ~15% and ~10%, respectively, and the intensity RI sensitivities are only ~200%/RIU and ~150%/RIU for the TM and TE modes in the C-L band, respectively. This is reasonable because the extinction spectrum of the GNSs is covering from 400 nm to 1600 nm, with the absorption coefficient gradually declining when the wavelength changes from 800 nm to 1600 nm [Fig. 2(b)], thus leading to the spectral and SRI effects of the TM and TE modes induced by the GNSs at the longer wavelength being weaker than those at the shorter wavelength.

In conclusion, we have studied the spectral effects and SRI sensing properties of the ExTFG induced by plasmonic GNSs with a large size (~155 nm). The wavelength and intensity RI sensing characteristics of the GNS-immobilized ExTFG sensor have been demonstrated. Experimental results reveal that the spectral effects originate from the coupling between the GNSs and the ExTFG cladding modes. The enhancement of the wavelength RI sensitivity for the TM mode stemming from the GNSs is relatively larger than that for the TE mode. The intensity attenuations of the TM and TE peaks are environmentally sensitive as a result of the modulation of the GNSs to the $\mathrm{Im}(n_{\mathrm{eff}})$ of the cladding modes by the SRI. The above spectral effects of the GNS immobilized on the ExTFG are polarization independent but wavelength dependent, which would become weaker when the resonance dual-peak is at a relatively longer wavelength. The proposed LSPR sensor based on GNS-immobilized ExTFG may provide a high performance biosensing platform by cross-linking the fiber or the particle surface with appropriate molecules or bioreceptors, which has the added advantages of a more robust structure and easier fabrication than the microfiber and side-polished fiber structure. In addition, the interrogation unit can be very cost efficient and the intensity RI sensitivity can be further improved simultaneously if the intensity measurement scheme with a single wavelength is adopted. According to the excitation mechanism of the LSPR effect of large-size GNSs by using the ExTFG platform, in the future, our research will also focus on improving the spectral effects and RI sensitivity by either using the cladding mode of the ExTFG near or covering the absorption peak (~780 nm) of the plasmonic GNSs or by using the ExTFG with a smaller core/cladding diameter.

References

1. Y. Huang, Z. Tian, L. P. Sun, D. Sun, J. Li, Y. Ran, and B. O. Guan, Opt. Express **23**, 26962 (2015).
2. Y. Wu, B. C. Yao, A. Q. Zhang, Y. J. Rao, Z. G. Wang, Y. Cheng, Y. Gong, W. Zhang, Y. F. Chen, and K. S. Chiang, Opt. Lett. **39**, 1235 (2014).
3. D. K. C. Wu, B. T. Kuhlmey, and B. J. Eggleton, Opt. Lett. **34**, 322 (2009).
4. S. Sridevi, K. S. Vasu, S. Sampath, S. Asokan, and A. K. Sood, J. Biophotonics **9**, 760 (2016).
5. B. C. Yao, Y. Wu, D. J. Webb, J. H. Zhou, Y. J. Rao, A. Pospori, C. B. Yu, Y. Gong, Y. F. Chen, and Z. G. Wang, IEEE Photonics Technol. Lett. **27**, 2399 (2015).
6. G. Quero, M. Consales, R. Severino, P. Vaiano, A. Boniello, A. Sandomenico, and M. Giordano, Biosens. Bioelectron. **80**, 590 (2016).
7. B. Gu, W. Qi, J. Zheng, Y. Zhou, P. P. Shum, and F. Luan, Opt. Lett. **39**, 22 (2014).
8. B. B. Luo, S. X. Wu, W. G. Zou, Z. H. Zhang, M. F. Zhao, S. H. Shi, Y. Liu, X. F. Xi, Z. Zeng, W. W. Liang, Z. J. Yan, and L. Zhang, Biosens. Bioelectron. **86**, 1054 (2016).
9. T. Guo, J. Lightwave Technol. **35**, 3323 (2017).
10. C. Ribaut, M. Loyez, J. C. Larrieu, S. Chevineau, P. Lambert, M. Remmelink, R. Wattiez, and C. Caucheteur, Biosens. Bioelectron. **92**, 449 (2017).
11. J. Cao, T. Sun, and K. T. V. Grattan, Sens. Actuators B **195**, 332 (2014).
12. H. Y. Lin, C. H. Huang, G. L. Cheng, N. K. Chen, and H. C. Chui, Opt. Express **20**, 21693 (2012).
13. J. Cao, M. H. Tu, T. Sun, and K. T. Grattan, Sens. Actuators B **181**, 611 (2013).
14. B. Doherty, M. Thiele, S. Warren-Smith, E. Schartner, H. Ebendorff-Heidepriem, W. Fritzsche, and M. A. Schmidt, Opt. Lett. **42**, 4395 (2017).
15. S. Lepinay, A. Staff, A. Ianou, and J. Albert, Biosens. Bioelectron. **52**, 337 (2014).
16. J. J. Lao, L. Z. Han, Z. Wu, X. J. Zhang, Y. Y. Huang, Y. Tang, and T. Guo, J. Lightwave Technol. (2018).
17. N. N. Peter, I. S. Lim, D. Mott, H. Y. Park, B. Khan, S. Mishra, R. Sujakumar, J. Luo, and C. J. Zhong, J. Phys. Chem. C **111**, 6601 (2007).
18. J. Burgmeier, A. Feizpour, W. Schade, and B. M. Reinhard, Opt. Lett. **40**, 546 (2015).
19. K. Zhou, L. Zhang, X. Chen, and I. Bennion, Opt. Lett. **31**, 1193 (2006).
20. Z. Yan, H. Wang, C. Wang, Z. Sun, G. Yin, K. Zhou, Y. Wang, W. Zhao, and L. Zhang, Opt. Express **24**, 12107 (2016).
21. F. Tam, C. Moran, and N. Halas, J. Phys. Chem. B **108**, 17290 (2004).
22. Y. F. Xu, B. B. Luo, S. H. Shi, Y. Wang, X. Zou, J. Lu, P. Tang, and M. F. Zhao, in *Proceedings of IEEE 16th International Conference on Optical Communications and Networks* (2017).